# Extraction method and denoising performance analysis of diffuse spots and silhouettes in STORM

*T. Cheng [1,2*], D. Hu [1]*
*[1] School of Mechanical and Automotive Engineering, Guangxi University of Science and Technology, 268 Avenue Dong Huan, Chengzhong District, Liuzhou 545006, P. R. China;*
*[2] School of Artificial Intelligence, Guangxi Science and Technology Normal University, 966 Tiebei Avenue, Laibin 546199, P. R. China*
** Corresponding author*

***Abstract***

In super-resolution microscopy based on STORM (Stochastic Optical Reconstruction Microscopy), due to the diffraction phenomenon, photons emitted by fluorescent molecules form into diffuse spots in a raw image. The regions without diffuse spots in the raw image are referred to as silhouettes. The diffuse spot regions are crucial for assessing the quality of a raw image and achieving super-resolution imaging as conventional holistic evaluation methods, which fail to distinguish between diffuse spots and silhouettes, cannot reflect the quality of the diffuse spot regions. A mask-based image segmentation algorithm is proposed here to extract and separate the diffuse spots and silhouette regions. Through simulation experiments, the denoising characteristics of three-dimensional block matching filtering (BM3D) and wide spectrum denoising (WSD) in different regions under various noise levels are compared and analyzed, and important criteria for selecting denoising methods for raw images are provided. Experiments show that better denoising is achieved with WSD than BM3D in the diffuse spot regions, while BM3D performs better in the silhouette regions in low noise level.

*Keywords*: super-resolution microscopy; raw image; diffuse spots; silhouette; denoising.
*Citation*: Cheng T, Hu D. Extraction method and denoising performance analysis of diffuse spots and silhouettes in STORM. Computer Optics 2026; 50(4): 1732. doi:10.18287/COJ1732.

## *Introduction*

The exploration of the essence of life represents one of humanity's ultimate goals. Throughout history, humans have continually sought ways to delve deeper into the microscopic world, and microscopes have played a pivotal role in this endeavor. The resolution of the human eye is only 0.1 mm. In comparison, since its invention in the 16th century, the resolution of the microscope has been continuously improving - the resolution of optical microscopes had reached 0.2 μm. by the end of the 19th century. With the aid of microscopes, people could observe cells and their internal structures. In the 1930s, the advent of the electron microscope further increased the resolution to 50 nm., enabling the possibility of observing even more intricate cellular structures [1].

Despite the significant improvement in resolution that electron microscopes offer compared to optical microscopes, they also have their limitations. For example, electron microscopes are unable to image specific multicolor labeling and live cells. Conversely, optical microscopes can precisely compensate for the disadvantages of electron microscopes. Due to the diffraction characteristics of light and the limitations of the optical system's aperture, the resolution of microscopes is restricted below the Abbe limit [2]. The visible light range for naked eye is 400–750 nm. Even with visible light at a wavelength of 400 nm, a resolution of only 200 nm can be achieved. In other words, the resolution of conventional optical microscopes is essentially limited to the order of 200 nm, falling far short of the resolution precision required to observe subcellular structures such as mitochondria and centrosomes. Research in fields like biomedical science demands microscopes with even higher resolution. Therefore, super-resolution optical microscopes have emerged to meet this need [3 – 5, 11].

With the rapid development of biomedical science, materials science, and other fields, the demand for higher image resolution has been increasing. Super-resolution microscopy, as a technique capable of breaking through the optical diffraction limit, has become an important tool for studying the microscopic world. The imaging principles of super-resolution microscopy are mainly divided into two categories. The first category is based on single-molecule localization microscopy (SMLM) [6 – 7], including techniques such as photoactivated localization microscopy (PALM) [8]and stochastic optical reconstruction microscopy (STORM) [9 – 10, 18]. The second category is based on the modulation of the point spread function (PSF), which includes techniques such as stimulated emission depletion microscopy (STED) [12] and structured illumination microscopy (SIM) [13 – 14]. Although STORM can significantly enhance image resolution, its imaging quality is compromised by the noise, as different levels of the noise lead to varying localization errors. Therefore, if the noise can be effectively eliminated, the resolution of STORM can be greatly improved [11].

In super-resolution microscopy based on STORM, due to the diffraction phenomenon, Photons emitted by fluorescent molecules form into diffuse spots in a raw image [15 – 16]. The spatial position of the fluorescent molecules can be located by calculating the centroid of the diffuse spot or by fitting methods. Theoretically, the area of the diffuse spot is

infinitely large. The center region of the diffuse spot contains the most photons, which decrease in number as one moves outward from the center. When the radius of the diffuse spot reaches a certain critical value, the periphery of the diffuse spot becomes almost indistinguishable from the background. Therefore, diffuse spots have finite sizes in practice. The regions without diffuse spots in a raw image are referred to as the silhouette. Since there are no fluorescent molecules in the silhouette region, the diffuse spot regions hold a much more significant position than the silhouette regions in super-resolution microscopy, as the diffuse spots have a decisive impact on imaging quality and resolution.

Raw images often have various noises, which can affect our ability to read the information in the images [17 – 18, 20]. Conventional denoising method selection often employs holistic evaluation methods that do not distinguish between the diffuse spot regions and the silhouette regions, making it difficult to accurately assess the denoising effects and the performance differences of different denoising methods in the diffuse spot regions and the silhouette regions. However, the diffuse spot regions are crucial for evaluating the quality of the raw image and achieving super-resolution imaging. This paper proposes an image segmentation algorithm based on a mask. The mask generated by this algorithm can effectively extract and separate the diffuse spots and silhouettes from the raw image. Thus, it provides a basis for evaluating and selecting denosing algorithms for STORM.

## *1. Methods*

In the simulation, the raw images' point spread function (PSF) was modeled as a two-dimensional Gaussian function. The PSF parameters were rigorously defined, with its full width at half maximum (FWHM) calibrated to 239.286 nm and the corresponding standard deviation measured 101.615 nm. The pixel size of the raw image was 45.715 nm. To differentiate from the raw image pixels, the super-resolution image pixels were termed grids. The grid size of the super-resolution image was one quarter of the raw image's pixel size [18, 20].

The mask is a 13×13 0 – 1 matrix, as shown in Fig. 1. The raw image is essentially also a matrix, with its pixel values being the elements of the matrix. The diffuse spot regions and silhouette regions in the raw image can be extracted and separated using the mask. The diffuse spot radius is r and the unit is pixels. The method for generating the mask is shown in Tab .1 – Algorithm 1.

In Algorithm 1, C represents the mask matrix. Cij denotes the element located at the ith row and jth column of C. If the distance from Cij to the center element of C is greater than r, set Cij to 0; otherwise, set it to 1. The center element of C is located at row 7 and column 7. The mask matrix C generated according to Algorithm 1 is shown in Fig. 1.

Fig. 2*a* is the raw image of a single diffuse spot, whose size is 13×13 pixels. The red cross at the center of the image indicates the position of the fluorescent molecule. Fig. 2*b* is the grayscale image of the mask shown in Fig. 1. Fig. 2*c* represents the extracted diffuse spot region based on a diffuse spot radius of 3.5 pixels. In other words, it is the result of element-wise multiplication of the two matrices represented by Fig. 2*a* and Fig. 1. Fig. 2*d* shows the remaining silhouette region after the extraction of the diffuse spot region, which is the result of subtracting the matrix represented by Fig. 2*c* from the matrix represented by Fig. 2*a*.

*Tab. 1. Algorithm 1: Mask generative approach*

| Algorithm 1: Mask generative approach |
|---|
| Input: C, a mask matrix of all ones. Its size is 13×13.<br>r, diffuse spot radius.<br>Initialization: 1 <=i, j<=13.<br>Iteration 1: At the ith iteration, go through the following steps.<br>Iteration 2: At the jth iteration, go through the following steps.<br>If $\sqrt{\lvert i-7\rvert^2+\lvert j-7\rvert^2} > r$, $C_{ij}=0$. |
| Output: The mask matrix C. |

| | | | | | | | | | | | | |
|---|---|---|---|---|---|---|---|---|---|---|---|---|
| 0 | 0 | 0 | 0 | 0 | 0 | 0 | 0 | 0 | 0 | 0 | 0 | 0 |
| 0 | 0 | 0 | 0 | 0 | 0 | 0 | 0 | 0 | 0 | 0 | 0 | 0 |
| 0 | 0 | 0 | 0 | 0 | 0 | 0 | 0 | 0 | 0 | 0 | 0 | 0 |
| 0 | 0 | 0 | 0 | 0 | 1 | 1 | 1 | 0 | 0 | 0 | 0 | 0 |
| 0 | 0 | 0 | 0 | 1 | 1 | 1 | 1 | 1 | 0 | 0 | 0 | 0 |
| 0 | 0 | 0 | 1 | 1 | 1 | 1 | 1 | 1 | 1 | 0 | 0 | 0 |
| 0 | 0 | 0 | 1 | 1 | 1 | 1 | 1 | 1 | 1 | 0 | 0 | 0 |
| 0 | 0 | 0 | 1 | 1 | 1 | 1 | 1 | 1 | 1 | 0 | 0 | 0 |
| 0 | 0 | 0 | 0 | 1 | 1 | 1 | 1 | 1 | 0 | 0 | 0 | 0 |
| 0 | 0 | 0 | 0 | 0 | 1 | 1 | 1 | 0 | 0 | 0 | 0 | 0 |
| 0 | 0 | 0 | 0 | 0 | 0 | 0 | 0 | 0 | 0 | 0 | 0 | 0 |
| 0 | 0 | 0 | 0 | 0 | 0 | 0 | 0 | 0 | 0 | 0 | 0 | 0 |
| 0 | 0 | 0 | 0 | 0 | 0 | 0 | 0 | 0 | 0 | 0 | 0 | 0 |

*Fig. 1. A 13×13 mask matrix with a diffuse spot radius of 3.5 pixels.*
*Matrix elements within the radius value 1 and elements outside the radius value 0*

Although Fig. 2*a* presents a simplified case with only one diffused spot, raw experimental images generally exhibit significantly larger dimensions and contain numerous diffused spots. The spatial distribution and topological relationships among these diffuse spots demonstrate extreme complexity due to molecular interactions and imaging conditions. Specifically, the topological configurations between adjacent spots may manifest as four principal categories: disjoint (no spatial contact), adjacent (boundary connection), covers (complete overlap), and partial overlap. Through Tab. 2 – Algorithm 2 implementation, both these diffused spots and their corresponding silhouette regions can be effectively extracted from raw images. Notably, this algorithm demonstrates robust adaptability, being applicable not only to standard 13×13 pixel microscopic images containing isolated single molecules, but also maintaining effectiveness when processing larger-scale raw image data with multiple overlapping molecular clusters. This dual-scale compatibility ensures its practical value in various experimental scenarios.

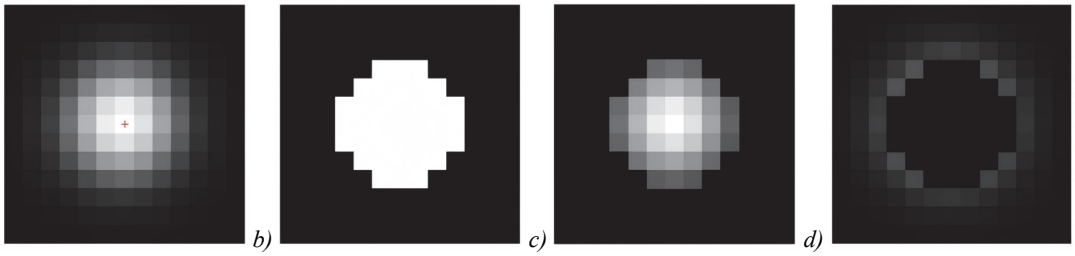


*Fig. 2. From left to right are the molecule raw image, masks, speckle image, and silhouette image and silhouette image. a) Raw image, b) mask, c) diffuse spot, d) silhouette*

*Tab. 2. Algorithm 2: Extraction methods of diffuse spots and silhouettes*

| Algorithm 2: Extraction methods of diffuse spots and silhouettes |
|---|
| Input:<br>R, a STORM raw image.<br>S, the corresponding super-resolution image.<br>N, the number of molecules in S.<br>r, the radius of a diffuse spot, in pixels.<br>Initialization:<br>C, a mask matrix with a radius r.<br>i and j, molecule coordinates in S, in grids.<br>r and c, molecule coordinates in R, in pixels. The r and c are the rounding of r/4 and c/4.<br>rc, the set of coordinates of the diffuse spot pixels in R. rc = Ø.<br>Iteration: At the kth iteration (the kth molecule, k<=N), go through the following steps.<br>blk, the 13×13 image block centered on the molecule coordinate (r and c).<br>blk = the hadamard product of blk and C.<br>pq, the position coordinate of the element of blk more than 0 in R.<br>rc = rc∪pq;<br>rc, the same data as in rc, but with no repetitions.<br>Processing:<br>Diffuse spots, set the pixel value of R whose coordinates do not belong to rc to 0.<br>Silhouette = R- Diffuse spots. |
| Output: |
| Diffuse spots and Silhouette. |

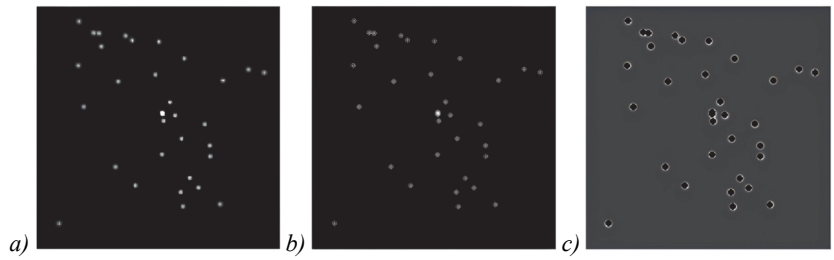


*Fig. 3. From left to right are raw images of fluorescent molecules, diffuse spots image and silhouette image. a) Raw image, b) diffuse spots image, c) silhouette image*

The diffuse spots can be extracted molecule by molecule with Algorithm 2, which is based on fluorescent molecules in the super-resolution image and the specified diffuse spot radius. The pixel values in non-diffuse spot regions are all 0, as shown in Fig. 3*b*. Fig. 3*c* is the silhouette, which results from subtracting Fig. 3*b* from Fig. 3*a*, and the pixel values in non-silhouette regions are all 0. To avoid the impact of 0-value regions in Figs. 4*b* and *c*, we only extract non-zero pixels when computing signal to noise ratio (SNR) and structural similarity index measure (SSIM) [19 – 21].

SNR reflects the overall quality of denoised raw images. SSIM, ranging from 0 to 1, assesses similarity between two images. Both SNR and SSIM evaluate denoising effectiveness on raw images.

$$SNR = 20 \times log_{10}\left(\frac{\|\mathbf{x}\|_2}{\|\mathbf{x_R}-\mathbf{x}\|_2}\right), \quad (1)$$

where $\mathbf{x}$ is a real signal, $\mathbf{x} \in \mathbf{R}^N; \|\cdot\|_2$ is the norm of a vector; and $\mathbf{x}_R$ denotes the other signal corresponding $\mathbf{x}$.

$$SSIM(x,y) = \frac{(2\mu_x\mu_y+c_1)(2\sigma_{xy}+c_2)}{(\mu_x^2+\mu_y^2+c_1)(\sigma_x^2+\sigma_y^2+c_2)}, \quad (2)$$

where $\mu_x$ and $\sigma_x$ represent the mean and the variance of image $x$, respectively. $\sigma_{xy}$ represents the covariance of image $x$ and $y$. $c_1 = (k_1 L)^2$ and $c_2 = (k_2 L)^2$. L is the dynamic range of pixel values. $k_1 = 0.01$, $k_2 = 0.03$。

## 2. Results and discussion

We create 20 and 500 simulated super-resolution image frames with known true molecular positions and corresponding raw image frames. The simulation involves stochastic molecular placement. The corresponding molecular densities are 6.304 μm$^{-2}$ (high-density) and 0.2522 μm$^{-2}$ (low-density). Each molecule emits 3000 photons, with a uniform background of 16 photons per pixel. We add Poisson and Gaussian noise to each raw image frame. The noise levels are categorized into low (Poisson noise only), medium (Poisson and Gaussian noise with 0.01 variance), and high (Poisson and Gaussian noise with 0.04 variance).

Different denoising methods have varying effects on the diffuse spots and silhouettes in raw images. To explore the impact of diffuse spot radius and noise level on denoising, experiments were designed with these two factors as independent variables and SNR/SSIM as dependent variables. Through these experiments, the denoising effects on raw images with different molecular densities, diffuse spots, and silhouettes were compared and analyzed [22]. The diffuse spot radius ranges from 1 to 7 pixels.

Fig. 4 shows mean curves of SNR and SSIM of high-density raw images, diffuse spots, and silhouettes at different noise levels, varying with diffuse spot radius. R, Rp, and Rs denote raw images, diffuse spots and silhouettes respectively; B, Bp, and Bs represent BM3D-denoised counterparts; W, Wp, and Ws stand for WSD-denoised ones, as in Fig. 4*a*. Though the areas of diffuse spots and silhouettes change with the diffuse spot radius, the raw image remains unchanged. Therefore, curves B, W, and R in Fig. 4 are horizontal. Since curves B and W in Figs. 4*b*-*g* are above R, both BM3D and WSD are effective denoising methods [23 – 24].

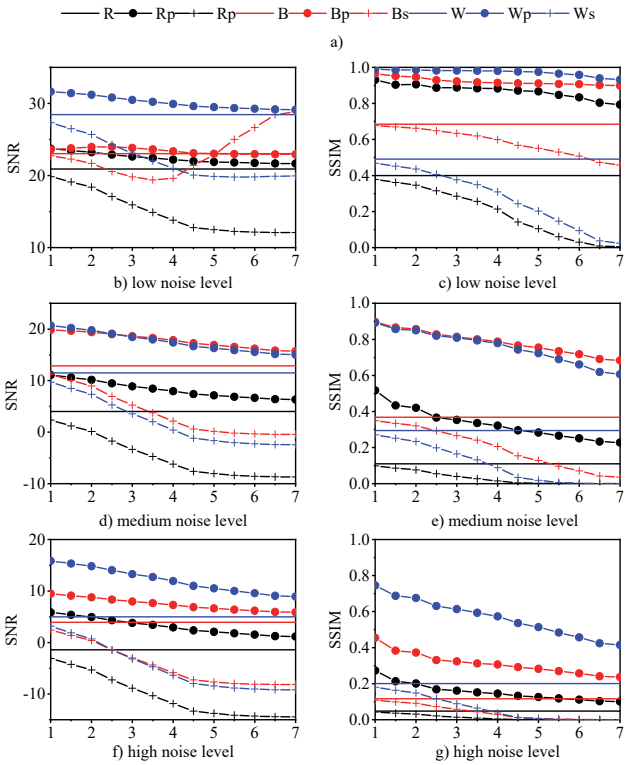


*Fig. 4. Denoising analysis of high-density raw images in low noise, medium noise and high noise levels. The abscissa is the diffuse spot radius*

By comparing Figs. 4*b*, *d*, and *f*, it can be observed that when the diffuse spot radius exceeds approximately 4, curve Rs tends to become horizontal. This indicates that beyond a diffuse spot radius of about 4, the impact of the diffuse spot

on the silhouette region becomes almost negligible. Therefore, a 4-pixel diffuse spot radius can serve as the critical value for distinguishing between diffuse spots and silhouette regions.

At low noise level, Fig. 4*b*'s curve W is above B, but Fig. 4*c*'s curve W is below B, making it difficult to tell which is better overall for raw image denoising between BM3D and WSD. In the diffuse spot region of Figs. 4*b* and *c,* curve Wp is always above Bp and the SNR is above about 7 dB. Therefore, the denoising effect of WSD is far better than BM3D in the diffuse spot region. When the diffuse spot radius is greater than approximately 4, curves Bs in Figs. 4*b* and *c* are above Ws. Thus, BM3D is better than WSD for denoising in the silhouette region.

At medium noise level, the curve B in Figs. 4*d* and *e* are all above W. BM3D outperforms WSD for raw image denoising. However, when the diffuse spot radius is about less than 4, the curve Wp in the diffuse spot region in Figs. 4*d* and *e* almost coincides with Bp. Thus, in the diffuse spot region, WSD has comparable denoising to BM3D. The curves Bs in Figs. 4*d* and *e* are all above the Ws. Therefore, in the silhouette region, BM3D has better denoising than WSD.

At high noise level, curves W in Figs. 4*f* and *g* are above B, indicating WSD outperforms BM3D in overall raw image denoising. In the diffuse spot region of Figs. 4*f* and *g*, curve Wp is always above Bp, with an SNR over 5dB higher and SSIM about 0.3 higher. Therefore, WSD is far better than BM3D for denoising in the diffuse spot region. When the diffuse spot radius is approximately greater than 4, curve Bs in Fig. 4*f* is slightly above Ws but nearly coincides with it; in Fig. 4*g*, curve Bs and Ws almost overlap. Thus, in the silhouette region, WSD has comparable denoising effect to BM3D.

In conclusion, in the diffuse spot region, both WSD and BM3D can denoise effectively. However, WSD show a better denoising effect than BM3D. In the silhouette region, both WSD and BM3D can effectively denoise. However, BM3D performs better than WSD. SNR and SSIM in the diffuse spot region show a monotonically decreasing trend as the diffuse spot radius increases.

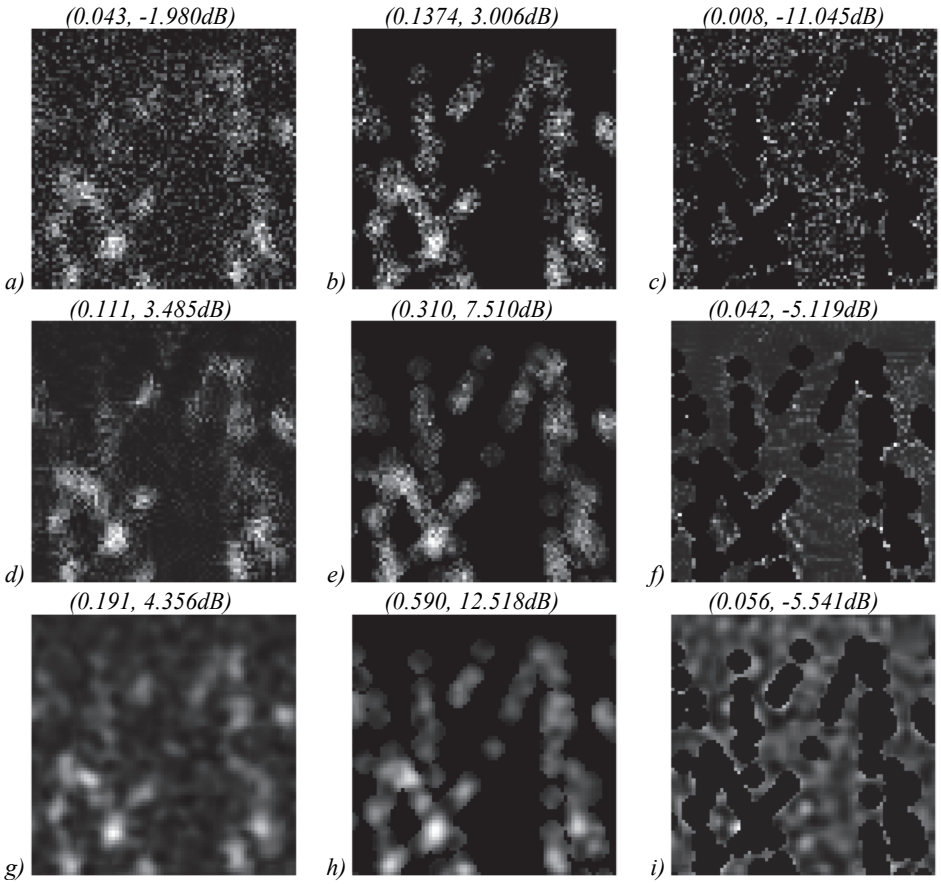


*Fig. 5. Denoising of high-density raw images in high noise level. a) RAW image, b) RAW diffuse spots, c) RAW silhouettes, d) BM3D image, e) BM3D diffuse spots, f) BM3D silhouettes, g) WSD image, h) WSD diffuse spots, i) WSD silhouettes*

Fig. 5 shows the denoising analysis results of using BM3D and WSD on a raw image frame with a diffuse spot radius of 3.5 pixels. Fig. 5*a* is the raw image before denoising, while Figs. 5*b* and *c* are the extracted diffuse spots and silhouettes. The number pairs above Figs. 5*a – c* indicate SSIM and SNR. Figs. 5*d – f* shows the denoised raw image, diffuse spots, and silhouette using BM3D, along with SSIM and SNR. Figs. 5*g – i* shows the corresponding results with WSD. Comparing Figs. 5*e* and *h*, we can see that the WSD-denoised diffuse spot region is smoother than BM3D, with SNR and SSIM improved from 0.31 and 7.51 dB to 0.59 and 12.518 dB. Thus, WSD outperforms BM3D in denoising the diffuse spot region.

Fig. 6 shows the curves of SNR and SSIM versus the diffuse spot radius for low-density raw images, diffuse spots, and silhouettes at different noise levels. As curves B and W in Figs. 6*a* – *g* are above R, both BM3D and WSD are effective denoising methods.

At low noise level, in Figs. 6*b* and *c*, curve B is above curve W. Therefore, BM3D is better than WSD in overall raw image denoising. In Fig. 6*c*, in the diffuse spot region, curve Wp is always above curve Bp, with an SNR at least 5 dB higher. In Fig. 6*c*, curve Wp in the diffuse spot region is slightly higher than curve Bp. Therefore, in the diffuse spot region, WSD shows a better denoising effect than BM3D. In Figs. 6*b* and *c*, curve Bs is above curve Ws. Thus, in the silhouette region, BM3D outperforms WSD in denosing.

At medium noise level, in Figs. 6*d* and *e*, curve B is above curve W, indicating BM3D outperforms WSD in overall raw image denoising. However, when the diffuse spot radius is less than 4, in Figs. 6*d* and *e*, curve Wp in the diffuse spot region is higher than curve Bp. Therefore, in the diffuse spot region, WSD is better than BM3D. In Figs. 6*d* and *e*, curve Bs is above curve Ws. Hence, in the silhouette region, BM3D surpasses WSD in denoising effect.

At high noise level, in Figs. 6*f* and *g*, curve W is above curve B, indicating WSD is better than BM3D in overall raw image denoising. In Figs. 6*f* and *g*, in the diffuse spot region, curve Wp is always above curve Bp, with an SNR over 7 dB higher and an SSIM about 0.4 higher. Therefore, in the diffuse spot region, WSD sign- ificantly outperforms BM3D in denoising. In Figs. 6*f* and *g*, curve Bs is below curve Ws. Hence, in the silhouette region, WSD has a better denoising effect than BM3D.

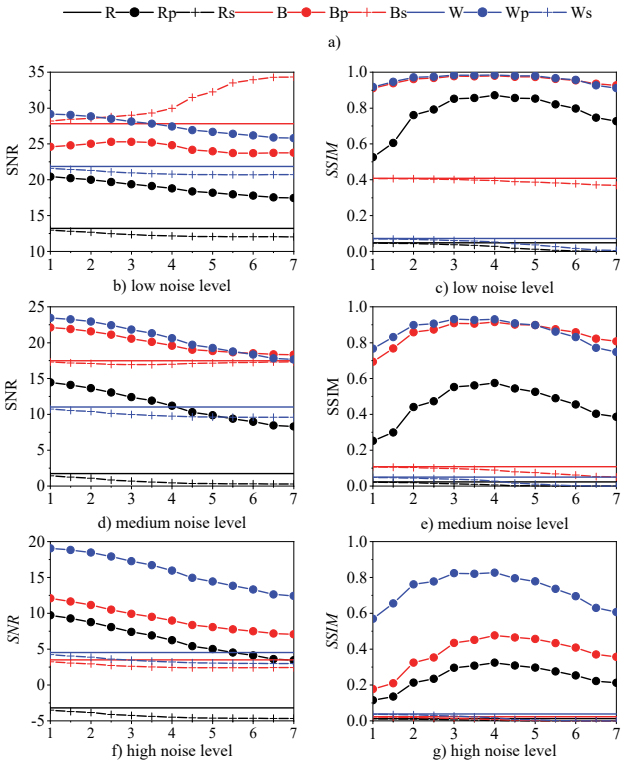


*Fig. 6. Denoising analysis of low-density raw images in low noise, medium noise and high noise levels. The abscissa is the diffuse spot radius*

By comparing Figs. 6*c*, *e*, and *g*, it can be found that the diffuse spot curves (Rs, Bs, and Ws) are all parabolic in shape, with their vertices located at a diffuse spot radius of approximately 4.

In general, both WSD and BM3D can effectively perform denoising in the diffuse spot region. However, WSD demonstrates superior denoising performance compared to BM3D. The SSIM for the diffuse spot region peaks when the diffuse spot radius is around 4. In the silhouette region, both WSD and BM3D are also effective. BM3D performs better than WSD at low and medium noise levels, while WSD surpasses BM3D at high noise level[18 – 19].

## *Conclusiones*

A mask-based image segmentation algorithm for the extraction and separation of diffuse spots and silhouette regions in STORM raw images is proposed. The critical value of 4 pixels for the diffuse spot radius can be used to distinguish between diffuse spots and silhouette regions. The mask-based image segmentation algorithm can effectively extract and separate diffuse spots and silhouette regions in the raw images, providing a basis for subsequent analysis of denoising performance and selection of denoising methods.

In the diffuse spot regions where the radius is not greater than 4 pixels, WSD outperforms BM3D in denoising effects. Especially at high noise level, the denoising effect of WSD is significantly better than that of BM3D. In the silhouette regions, BM3D generally outperforms WSD at low and medium noise levels. However, at high-noise level with low

density, WSD is better than BM3D. This finding breaks through the limitations of conventional holistic denoising evaluation and provides a basis for targeted denoising in different regions of a raw image. For instance, WSD can be preferentially adopted in diffuse spot regions, while BM3D denoising can be appropriately applied in silhouette regions.

***Acknowledgements***

The work was funded by Guangxi National Natural Science Foundation (2022GXNSFAA035593), National Natural Science Foundation of China (81660296, 41461082).

***References***

[1] Chua EYD, Mendez JH, Rapp M, Ilca SL, Tan YZ, Maruthi K, Kuang H, Zimanyi CM, Cheng A, Eng ET, Noble AJ, Potter CS, Carragher B. Better, faster, cheaper: recent advances in cryo–electron microscopy. Annu Rev Biochem 2022; 91: 1-32. doi:10.1146/annurev-biochem-032620-110705.

[2] Gallegos-Cerda SD, Hernández-Varela JD, Chanona-Pérez JJ, Arredondo Tamayo B, Méndez Méndez JV. Super-resolution microscopy and their applications in food materials: beyond the resolution limits of fluorescence microscopy. Food Bioprocess Technol 2023; 16(2): 268-288. doi:10.1007/s11947-022-02883-4.

[3] Möckl L, Moerner WE. Super-resolution microscopy with single molecules in biology and beyond—essentials, current trends, and future challenges. J Am Chem Soc 2020; 142(42): 17828-17844. doi:10.1021/jacs.0c08178.

[4] Liu S, Hoess P, Ries J. Super-resolution microscopy for structural cell biology. Annu Rev Biophys 2022; 51: 301-326. doi:10.1146/annurev-biophys-102521-112912.

[5] Qiao C, Li D, Liu Y, Zhang S, Liu K, Liu C, Guo Y, Jiang T, Fang C, Li N, Zeng Y, He K, Zhu X, Lippincott-Schwartz J, Dai Q, Li D. Rationalized deep learning super-resolution microscopy for sustained live imaging of rapid subcellular processes. Nat Biotechnol 2023; 41(3): 367-377. doi:10.1038/s41587-022-01471-3.

[6] Hugelier S, Colosi PL, Lakadamyali M. Quantitative single-molecule localization microscopy. Annu Rev Biophys 2023; 52: 139-160. doi:10.1146/annurev-biophys-111622-091212.

[7] Breton V, Nazac P, Boulet D, Danglot L. Molecular mapping of neuronal architecture using STORM microscopy and new fluorescent probes for SMLM imaging. Neurophotonics 2024; 11(1): 014414. doi:10.1117/1.NPH.11.1.014414.

[8] Jensen LG, Hoh TY, Williamson DJ, Griffié J, Sage D, Rubin-Delanchy P, Owen DM. Correction of multiple-blinking artifacts in photoactivated localization microscopy. Nat Methods 2022; 19(5): 594-602. doi:10.1038/s41592-022-01463-w.

[9] Huang L, Zhang J, Wu Z, Zhou L, Yu B, Jing Y, Qu J. Revealing the structure and organization of intercellular tunneling nanotubes (TNTs) by STORM imaging. Nanoscale Adv 2022; 4(20): 4258-4262. doi:10.1039/D2NA00415A.

[10] Chen H, Yan G, Wen MH, Brooks KN, Zhang Y, Huang PS, Chen TY. Advancements and practical considerations for biophysical research: navigating the challenges and future of super-resolution microscopy. Chem Biomed Imaging 2024; 2(5): 331-344. doi:10.1021/cbmi.4c00019.

[11] Le Bourdellès G, Mercier L, Roos J, Bancelin S, Nägerl UV. Impact of a tilted coverslip on two-photon and STED microscopy. Biomed Opt Express 2024; 15(2): 743-752. doi:10.1364/BOE.510512.

[12] Li X, Wu Y, Su Y, Rey-Suarez I, Matthaeus C, Updegrove TB, Wei Z, Zhang L, Sasaki H, Li Y, Guo M, Giannini JP, Vishwasrao HD, Chen J, Lee SJ, Shao L, Liu H, Ramamurthi KS, Taraska JW, Upadhyaya A, La Riviere P, Shroff H. Three-dimensional structured illumination microscopy with enhanced axial resolution. Nat Biotechnol 2023; 41(9): 1307-1319. doi:10.1038/s41587-022-01651-1.

[13] Chen B, Chang BJ, Roudot P, Zhou F, Sapoznik E, Marlar-Pavey M, Hayes JB, Brown PT, Zeng CW, Lambert T, Friedman JR, Zhang CL, Burnette DT, Shepherd DP, Dean KM, Fiolka RP. Resolution doubling in light-sheet microscopy via oblique plane structured illumination. Nat Methods 2022; 19(11): 1419-1426. doi:10.1038/s41592-022-01635-8. [web:370][web:372]

[14] Adams JK, Yan D, Wu J, Boominathan V, Gao S, Rodriguez AV, Kim S, Carns J, Richards-Kortum R, Kemere C, Veeraraghavan A, Robinson JT. In vivo lensless microscopy via a phase mask generating diffraction patterns with high-contrast contours. Nat Biomed Eng 2022; 6(5): 617-628. doi:10.1038/s41551-022-00851-z.

[15] Xiong Z, He W, Wang W, Fu Y. Super-resolution lensless imaging system based on a fast anti-diffraction algorithm. Opt Express 2023; 31(23): 37395-37407. doi:10.1364/OE.500097.

[16] Izadi S, Sutton D, Hamarneh G. Image denoising in the deep learning era. Artif Intell Rev 2023; 56(7): 5929-5974. doi:10.1007/s10462-022-10305-2.

[17] Jang H, Li Y, Fung AA, Bagheri P, Hoang K, Skowronska-Krawczyk D, Chen X, Wu JY, Bintu B, Shi L. Super-resolution SRS microscopy with A-PoD. Nat Methods 2023; 20(3): 448-458. doi:10.1038/s41592-023-01779-1.

[18] Sara U, Akter M, Uddin MS. Image quality assessment through FSIM, SSIM, MSE and PSNR—a comparative study. J Comput Commun 2019; 7(3): 8-18. doi:10.4236/jcc.2019.73002.

[19] Mannam V, Zhang Y, Zhu Y, Nichols E, Wang Q, Sundaresan V, Zhang S, Smith C, Bohn PW, Howard SS. Real-time image denoising of mixed Poisson–Gaussian noise in fluorescence microscopy images using ImageJ. Optica 2022; 9(4): 335-345. doi:10.1364/OPTICA.448287. [web:373]

[20] Omara AN, Salem TM, Elsanadily S, Elsherbini MM. SSIM-based sparse image restoration. J King Saud Univ Comput Inf Sci 2022; 34(8): 6243-6254. doi:10.1016/j.jksuci.2021.07.024.

[21] Chaudhary J, Phulia A, Pandey AK, Sharma PD, Patel C. Denoising Tc-99m DMSA images using denoising convolutional neural network with comparison to a block matching filter. Nucl Med Commun 2023; 44(8): 682-690. doi:10.1097/MNM.0000000000001712.

[22] Cheng T, Chen D, Li H. Wide spectrum denoising (WSD) for super-resolution microscopy imaging using compressed sensing and a high-resolution camera. J Phys Conf Ser 2020; 1651: 012177. doi:10.1088/1742-6596/1651/1/012177.

[23] Yahya AA, Tan J, Su B, Hu M, Wang Y, Liu K, Hadi AN. BM3D image denoising algorithm based on an adaptive filtering. Multimed Tools Appl 2020; 79: 20391-20427. doi:10.1007/s11042-020-08815-8.

***Authors' information***

**Tao Cheng,** Doctor of Technical Sciences, Professor, Professor of School of Mechanical and Automotive Engineering of Guangxi University of Science and Technology. Research interests: medical imaging and image processing. He is also the **corresponding author** of this paper. E-mail: *ctnp@163.com*

**Di Hu,** Master's student of School of Mechanical and Automotive Engineering of Guangxi University of Science and Technology. Research interests: microscopy and image processing. E-mail: *18977447757@163.com*

*Received on May 19, 2025.* *The final version – June 15, 2025.*